Steel and Composite Structures, *Vol. 28, No. 5 (2018) 573-588*
DOI: https://doi.org/10.12989/scs.2018.28.5.573

Behavior of polygonal concrete-filled steel tubular stub columns under axial loading

Tao Zhang [1,2], Fa-xing Ding [*1], Liping Wang [1,2], Xue-mei Liu [3] and Guo-shuai Jiang [1]

[1] *School of Civil Engineering, Central South University, Changsha 410075, P.R. China*
[2] *Engineering Technology Research Center for Prefabricated Construction Industrialization of Hunan Province, 410075, P.R. China*
[3] *School of Civil Engineering and Built Environment, Queensland University of Technology, Brisbane, QLD 4000, Australia*

(*Received December 30, 2017, Revised May 16, 2018, Accepted June 25, 2018*)

Abstract. The objective of this paper is to investigate the mechanical performances of polygonal concrete-filled circular steel tubular (CFT) stub columns under axial loading through combined experimental and numerical study. A total of 32 specimens were designed to investigate the effect of the concrete strength and steel ratio on the compressive behavior of polygonal CFT stub columns. The ultimate bearing capacity, ductility and confinement effect were analyzed based on the experimental results and the failure modes were discussed in detail. Besides, ABAQUS was adopted to establish the three dimensional FE model. The composite action between the core concrete and steel tube was further discussed and clarified. It was found that the behavior of CFT stub column changes with the change of the cross-section, and the change is continuous. Finally, based on both experimental and numerical results, a unified formula was developed to estimate the ultimate bearing capacity of polygonal CFT stub columns according to the superposition principle with rational simplification. The predicted results showed satisfactory agreement with both experimental and FE results.

Keywords: polygonal concrete-filled steel tubular (CFT) stub column; ultimate bearing capacity; strain ratio; composite action; compressive behavior

1. Introduction

With the advantages of high load bearing capacity, high ductility, excellent seismic behavior, and fast construction, the concrete-filled steel tubular (CFT) column have been proposed as a new type of composite structures and widely used in building and bridges construction practice, even in regions of high seismic risk. This is because CFT columns ideally combine the advantages of both steel and core concrete (Ellobody 2013a, b, Jamaluddin *et al*. 2013, Kim *et al*. 2013). The concrete infill adds stiffness to the steel tube and prevents the occurrence of local buckling, while the steel tube improves the compressive strength and deformation performance of the core concrete. On the other hand, CFT stub columns require no reinforced cage and no formwork, in which the external steel tubes may act as permanent and integral formworks which lead to reduction in labour costs, materials and construction time. Thus, researchers and engineers are paying more attention on CFT structures (Zha *et al*. 2013, Wang and Chang 2013, Xiamuxi and Hasegawa 2011, Hua *et al*. 2014, Yang *et al*. 2014).

The compressive behavior of CFT stub columns is fundamental and important characteristic in practice engineering. So far, the large numbers of experimental and numerical studies have been conducted on the compressive behavior of CFT stub columns with different cross-sections (Huang *et al*. 2012, Uenaka 2014, Aslani *et al*. 2015, El-Heweity 2012, Wan and Zha 2016, Park and Choi 2013, Yang *et al*. 2014). Liang (2017) presented a new numerical model for predicting the structural performance of circular DCFST short columns under axial compression and a design formula is proposed. A new unified design formula for calculating the composite compressive strength of the axially loaded circular concrete filled double steel tubular short and slender columns based on the limit equilibrium theory, the cylinder theory and the "Unified theory" under axial compression is presented by Wan and Zha (2016). Wang *et al*. (2017) conducted an experimental and theoretical study on the compressive strength, compressive stiffness and deformation capacity of the CFST columns, and the capacity reduction factors for the steel and concrete materials are calibrated. Xu *et al*. (2016) carried out a series of compressive test of the hexagonal concrete-filled steel tubular (CFST) columns, and the FE model is used to conduct the full range analysis on the load versus deformation relation, internal force distribution and stress development. Tao *et al*. (2013) developed finite element models to study the compressive performance of CFT stub column. Evirgen *et al*. (2014) carried out the experiments on CFT stub columns and investigated the effect of some parameters on the ultimate loads, axial stress, ductility and buckling behavior. El-Heweity (2012) studied the mechanical properties of circular concrete-filled high strength steel columns by the finite element method and it was found that the use of high-strength tube in CFT columns was not promising. Uenaka (2014) conducted an

*Corresponding author, Ph.D., Professor,
E-mail: dinfaxin@csu.edu.cn

ISSN: 1229-9367 (Print), 1598-6233 (Online)

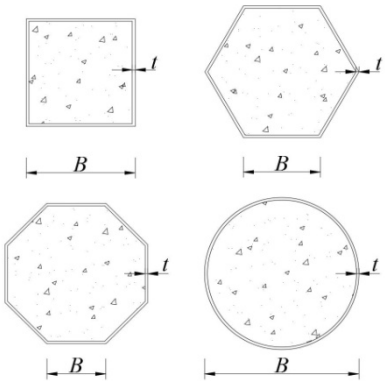

Fig. 1 Cross-section of CFT stub columns

experimental investigation on the behavior of concrete filled elliptical/oval steel tubular stub columns and a method for predicting the ultimate loading capacity was proposed. However, the composite action between the steel tube and core concrete could change and it was associated with the change of the cross-section for CFT stub columns. Hence, the change of the composite action needs to be further clarified.

To meet the requirement of architectural esthetics, the CFT stub columns can be designed with different geometries including polygonal shape, as shown in Fig. 1. However, to the authors' best knowledge, there is very limited research reported on the compressive performance of the polygonal CFT stub columns. The change of the

Table 1 Geometric properties and characteristics of specimens

Cross-section	Specimen ID	$B\times t$ (mm)	L (mm)	f_{cu} (MPa)	f_y (MPa)	ρ	$N_{u,\mathrm{Exp}}$ (kN)	DI
Square	S1	300×3.75	900	39.3	311	0.049	4370	2.7
	S2	300×3.70		57.4		0.049	5570	2.4
	S3-A	200×3.69	600	39.3		0.072	2160	5.9
	S3-B	201×3.74				0.073	2090	6.0
	S4-A	200×3.75		57.4		0.074	2500	4.4
	S4-B	200×3.74				0.073	2610	4.3
	S5-A	251×3.75	750	40.4	327	0.063	3131	1.4
	S5-B	251×3.73				0.063	2832	1.3
Hexagonal	HST1-A	196×3.73	1200	39.3	311	0.044	4947	3.8
	HST1-B	198×3.71				0.043	4618	3.3
	HST2-A	196×5.78			321	0.067	6001	7.2
	HST2-B	198×5.96				0.068	6041	7.6
	HST3-A	197×3.72		57.4	311	0.043	6827	3.2
	HST3-B	198×3.76				0.043	6803	3.3
	HST4-A	199×5.89			321	0.067	7079	5.8
	HST4-B	196×5.81				0.067	7289	6.4
Octagonal	OST1-A	201×3.85	1500	39.3	311	0.032	9297	6.8
	OST1-B	199×3.98				0.033	9311	3.1
	OST2-A	200×6.02			321	0.049	10502	8.0
	OST2-B	197×5.89				0.049	10713	7.7
	OST3-A	200×3.92		57.4	311	0.032	12362	4.0
	OST3-B	199×4.02				0.033	12357	4.0
	OST4-A	197×5.88			321	0.049	12992	8.1
	OST4-B	198×5.98				0.049	13263	5.3
Circular	C1-A	300×3.70	900	39.3	311	0.056	3780	6.2
	C1-B	300×3.76				0.056	3540	6.3
	C2-A	300×3.74		57.4		0.056	4896	4.1
	C2-B	300×3.87				0.056	4976	3.9
	C3-A	251×3.70	750	40.4	327	0.058	3023	5.96
	C3-B	250×3.69				0.062	3265	5.81
	C4-A	251×5.51			299	0.086	3556	6.53
	C4-B	252×5.74				0.089	3661	6.79

cross-section for CFT stub columns is continuous, but the change of the design formulas for calculating the ultimate bearing capacity is not. For CFT stub column with the same cross-section, there are many formulas from different standards and their expression forms are different, which have prevented them from being widely applied in the engineering practice. It is a challenge and important issue for designers and engineers who require a unified and precise design formula to estimate the ultimate strength on the polygonal CFT stub columns. Therefore, it is necessary that a unified formula is established, which is an effective way to calculating the ultimate bearing capacity of CFT stub columns.

Experimental study have been a basic analysis method on investigating the behavior and predicting the response of steel-concrete composite structural, while finite element method is becoming more and more important for simulating those difficult or/and complex cases. Chang *et al*. (2013, 2014) carried out a numerical study on the behavior of the composite structures based on the ABAQUS standard solver. Hassanein *et al*. (Hassanein *et al*. 2013, Hassanein and Kharoob 2014) performed finite element analysis to investigate the mechanical performance of circular concrete-filled double skin tubular short columns with external stainless steel tubes under axial loading. FE models were established by Pagoulatou *et al*. (2014) and a new formula was proposed to evaluate the strength of the double-skin specimens. Therefore, the compressive behavior of CFT stub columns will be investigated through combined the experimental and software ABAQUS in this paper.

With consideration of the research gaps mentioned above, this paper aims to develop a unified and precise formula for predicting the ultimate bearing capacity, and to investigate the behavior of the polygonal CFT stub columns under axial loading. More specifically, based on the experimental and numerical research from our team (Ding *et al*. 2011, 2014, 2017, Liu *et al*. 2016), the main contents of this paper are as follows: (1) Compression tests on 32 specimens with varied cross-section are conducted to investigate the effect of the concrete strength and steel ratio on the behavior of CFT stub columns. (2) ABAQUS is used to establish the finite element model and investigate the compressive behavior of the polygonal CFT stub columns. (3) Based on the limit equilibrium method, a simplified formula for predicting the ultimate bearing capacity of the polygonal CFT stub columns is proposed.

2. Experimental investigation

2.1 Test specimens and materials

A total of 32 CFT specimens were designed in this study, including 8 square, 8 hexagonal, 8 octagonal and 8 circular specimens. The cross-sectional dimensions of CFT specimens are shown in Fig. 1. The details of specimens are given in Table 1, where B is the outer edge length of the cross-section and also the diameter of the circular cross-section; t is the wall thickness of steel tube; L is the height of the specimen; f_{cu} is the cube strength of strength; and f_y is the yield strength of steel. ρ is the steel ratio, which is defined as the steel area divided by the total cross-sectional area. $N_{u,\exp}$ is the ultimate bearing capacity of specimen. *DI* refers to the ductility of specimen.

The steel tubes were all manufactured from Q235 steel plates. Butt welds were used according to the standard GB 50017-2003 and it was also necessary to ensure that the ends of the steel grooves (as the sites of welding) were smooth after welding.

For better observation and record of deformation and failure of the specimens, red paint was sprayed on the outer surface of the steel tubes and 50 mm × 50 mm white grids were plotted on the painted surface. Before concrete casting, the cover plate was welded to one end of the steel tube and then make the steel tube erect. And then concrete was placed from the top of the specimens, and carefully vibrated using a vibrator to distribute the concrete evenly inside the tube. Finally the upper surface of concrete was leveled to the same level with the steel tube. Meanwhile, the standard concrete cubes with a dimension of 150mm were prepared and cured under the same condition as the concrete used in columns. The concrete surface of the column specimens was polished with grinder after the concrete was hardened. And then a layer of epoxy resin binder was daubed to level the end surface. After that, the steel cover plates were welded to the end of the specimens to ensure that the load was applied to the steel tube and core concrete, simultaneously.

2.2 Materials

Before testing the columns, material testing, including concrete and steel, was conducted to obtain the respective mechanical properties according to the corresponding standard methods. Mild steel was used in the study and tensile coupon tests were conducted with three specimens to obtain the tensile properties according to the standard GB/T228-2002. The obtained yield strength, ultimate tensile strength, elastic module and Poisson's ratio of steel are listed in Table 2. In addition, three types of concrete are used and the cubic compressive strength (f_{cu}) of concrete was obtained from the testing of the concrete cubes in accordance with the standard GB/T50081-2002. The detailed material properties were listed in Table 2.

Table 2 Properties of steel and concrete

Material	t (mm)	f_y (Mpa)	f_u (Mpa)	E_s (Mpa)	v_s
Steel	4 mm	299	448	2.07×105	0.289
	4 mm	311	460	2.09×105	0.292
	6 mm	321	480	2.02×105	0.254
	4 mm	327	460.3	2.08×105	0.293
Material	Type	f_c (Mpa)	f_{cu} (Mpa)	E_c (Mpa)	v_c
Concrete	C40	29.2	39.3	3.07×104	0.21
	C60	45.1	57.4	3.05×104	0.25
	C40	29.5	40.4	3.08×104	0.23

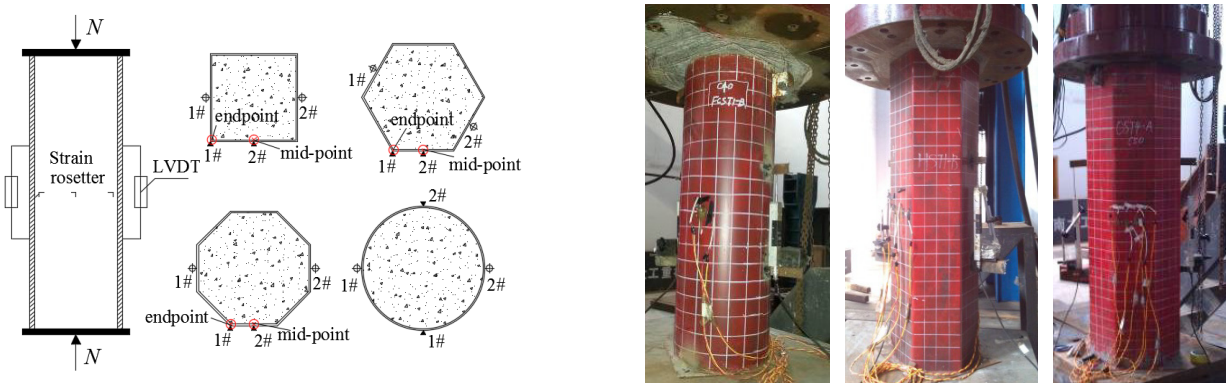

(a) Schematic view (b) Experimental setup

Fig. 2 Experimental instrumentation for all specimens

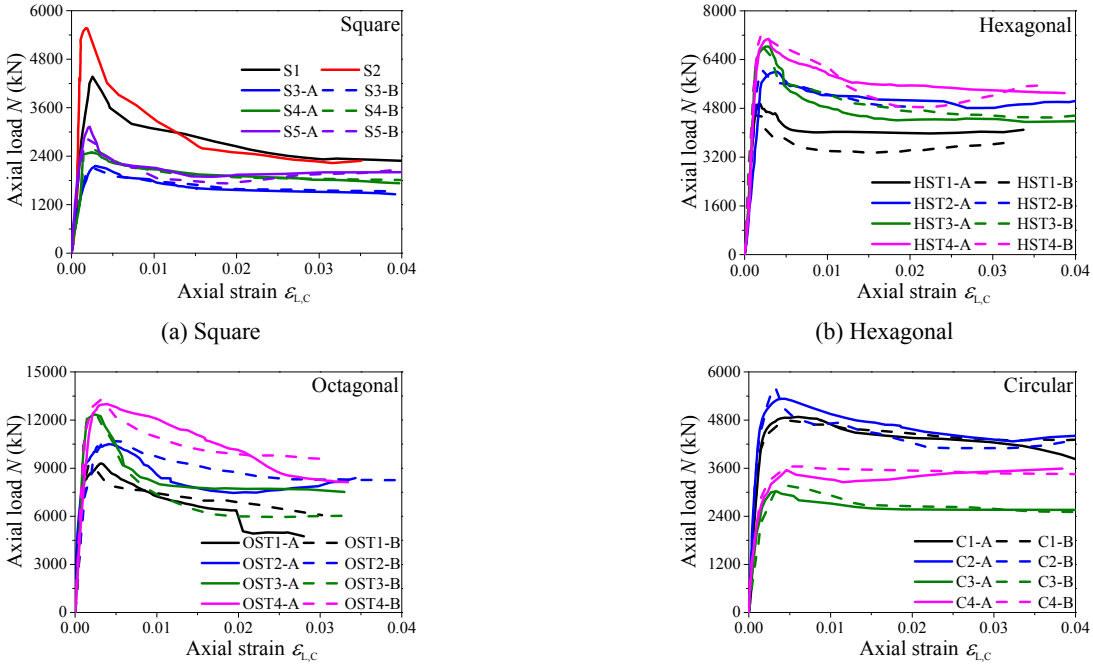

(a) Square (b) Hexagonal

(c) Octagonal (d) Circular

Fig. 3 Comparison of axial load vs. strain curves of specimens

2.3 Experimental setup and instrumentation

Compressive experiments on the specimens were conducted using a 2000-ton tri-axial stress testing machine in the National Engineering Laboratory for high-speed railway construction technology of Central South University. In order to accurately measure the deformation, strain rosettes were attached on the external surface of the steel tube at the mid-height and two LVDTs were installed at the mid-height of the external surface, as shown in Fig. 2(a). Load-strain curves were acquired by a DH3818 static strain measurement system and load-deformation curves were collected from electronic transducers and data acquisition system.

The compressive load was applied on the top of the specimens using a load control mode. The load was increased at a step of 1/20 of the expected ultimate load in the elastic stage. The load was applied to the specimen by means of displacement control with an increment of 0.2 mm/m after the load reached about 60% of the expected ultimate bearing capacity. Each loading step took 3-5 min. When the ultimate load was approached, specimens were loaded at a step of 0.5 mm and maintained 5 min. The tests were stopped when the axial strain reached 0.04 which was the largest strain of the specimens. The loading period for each specimen lasts about 2 hours.

3. Experimental results and discussion

3.1 Axial load vs. strain curves

Based on the test observation and the obtained axial load vs. strain curves, as shown in Fig. 3, the compressive process of the specimens are divided into three stages until

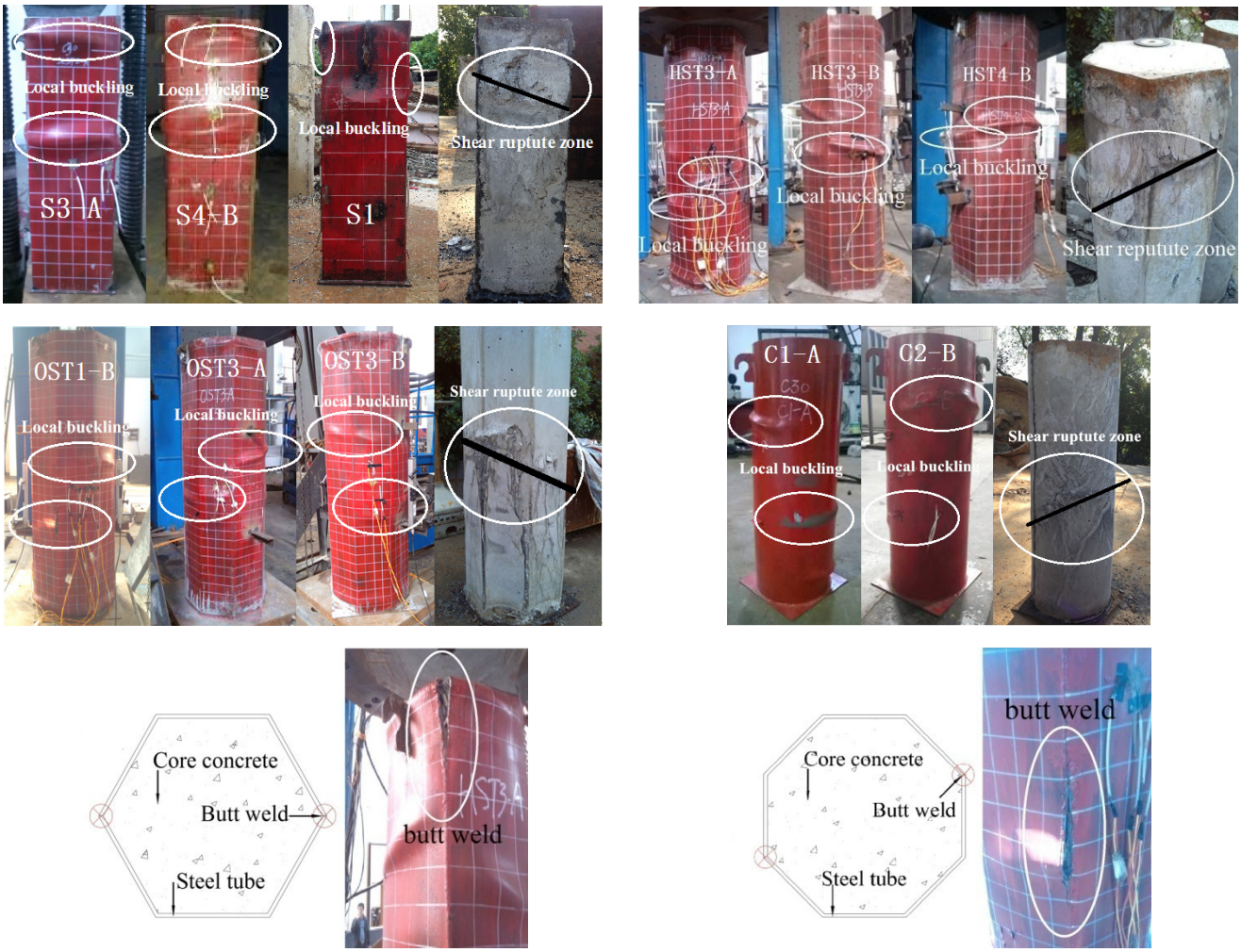

Fig. 4 Typical failure modes for test specimens

failure including elastic stage, elastic-plastic stage, and plastic stage.

Elastic stage: All specimens were in elastic phase, indicating that the axial load vs. strain curve was close to linearity. It can be found from the Fig. 3 that the compressive stiffness of the specimens in this stage was greater than that in others stages, consequently the axially elastic displacement was very limited.

Elastic-plastic stage: For all specimens, when the imposed load reached about 60% of the ultimate load, the steel tube began to yield and the load vs. strain curves diverged significantly from its initial linearity. In this stage, the visible local buckling of steel tube initially appeared near to the upper end of the specimens due to the end effect and later on generated in the middle where local bucking developed sharply. When the load reached the ultimate loading capacity, obvious buckling on the steel tube was observed.

Plastic stage: After reaching the ultimate load, the load bearing capacity of the specimens decreased rapidly with the continuously increased of displacement, due to the crush of the core concrete and the further bucking of the steel tube, as shown in Fig. 4. It can be seen from Fig. 3 that the load bearing capacity of the specimens with higher steel ratio declined slower (higher ductility) than that with lower steel ratio (lower ductility). The results show that the increased steel ratio can effectively improve the ductility of specimens.

3.2 Failure modes

Fig. 4 shows the failure mode of the typical tested specimens. It can be seen from Fig. 4, the typical failure modes of steel tubes are local outward buckling and associated with shear failure of in-filled concrete.

Two obvious local buckling were observed at different heights on the opposite sides of the steel tube, and there is a visible shear plane occurred between the local buckling, as shown in Fig. 4. After the test terminated, the outer steel tube of the specimens was cut open and removed from the core concrete to examine the failure mode of the core concrete. It can be seen that there were inclined shear rupture zones or/and even crushes in the core concrete, but the core concrete remains its entirety due to the confinement effect of the outer steel tube, as shown in Fig. 4. The results illustrate that the outer steel tube can't effectively prevent the generation of shear sliding crack in the core concrete. Besides, it can be found that the local buckling of the steel tube is gradually reduced with the increase of the number of edges. This is because the

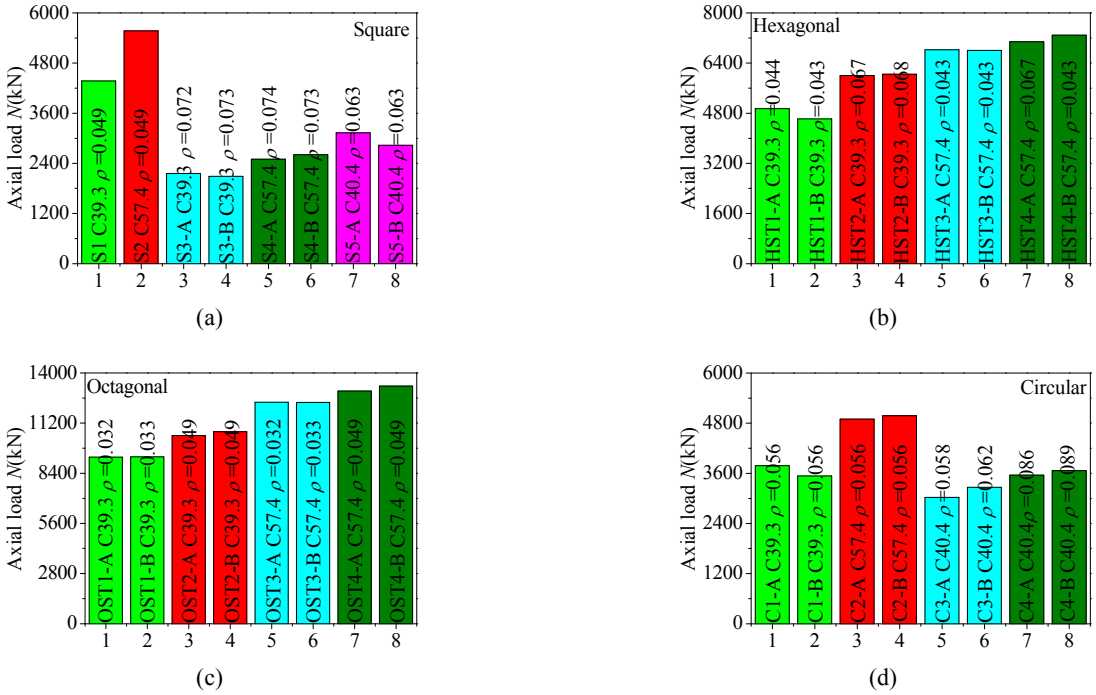

Fig. 5 Comparison of ultimate bearing capacity for all specimens

confinement effect of the steel tube on the core concrete is strengthened due to the increase of the cross-section. As the ductility of butt weld was poorer than that of the steel tube, weld failure along the butt welds was observed, as shown in Fig. 4.

3.3 Parametric study

To obtain deeper understanding on the behavior of CFT stub columns under axial loading, the following will take the octagonal specimens as examples to discuss the effect of steel ratio and concrete strength.

3.3.1 Steel ratio

The steel ratio (ρ) is defined as the steel area (A_s) divided by the total cross-sectional area (A_{sc}). The steel ratio is an important factor for CFT stub columns which has been tentatively investigated in previous research work. Therefore, the steel ratio affecting behavior of CFT stub columns will be discussed in this section.

Fig. 5 shows the experimental results of the ultimate bearing capacity of all specimens. The steel ratio is the variable, while other parameters are kept the same as mentioned above. Compared to the OST1 specimens, the average ultimate bearing capacity of the OST2 specimens was improved by 55.2%, with the increase of steel ratio from 3.3% to 4.9%. Besides, compared to the OST3 specimens, the average ultimate bearing capacity of the OST4 specimens was slightly improved by 6.2%, with the increase of steel ratio from 3.3% to 4.9%. Therefore, it is concluded that increased steel ratio is an effective way to enhance the ultimate bearing capacity, especially for CFT stub columns with low-grade concrete. Similar conclusion can be drawn from Fig. 5, where the cross-section of the specimens is in other shapes.

3.3.2 Concrete strength

The concrete strength is another important parameter affecting behavior of CFT stub columns as presented in Fig. 5. The concrete strength was the variable and other parameters were kept the same as mentioned above. In comparison to the OST1 specimens, the average ultimate bearing capacity of the OST3 specimens was improved by 32.8% with a 46.1% increase of concrete strength. In addition, compared to the OST2 specimens, the average ultimate bearing capacity of the OST4 specimens was improved by 23.8% with a 46.1% increase of concrete strength. In summary, the ultimate bearing capacity increases with the increase of concrete strength. Similar conclusion can be drawn from Fig. 5 for the specimens with other cross-sections.

3.3.3 Ductility

In order to investigate the effect of various parameters on the ductility of the specimens, a ductility index (*DI*) (Ding *et al*. 2014) is introduced in this study, which is defined as follows

$$DI = \frac{\varepsilon_{0.85}}{\varepsilon_{\mathrm{b}}} \tag{1}$$

where $\varepsilon_{0.85}$ is the axial strain when the load falls to 85% of the ultimate load, ε_b is equal to $\varepsilon_{0.75}$/0.75. $\varepsilon_{0.75}$ is the axial strain when the load attains of 75% the ultimate load in the pre-peak stage.

Fig. 6 shows comparison of the *DI* calculated by Eq. (1) for all tested specimens, where a higher *DI* value indicates a slower process of load reduction after the ultimate state. Compared to the OST1 specimens, the average *DI* of the OST2 specimens was improved by 59%, with the increase of steel ratio from 3.3% to 4.9%. Moreover, in comparison

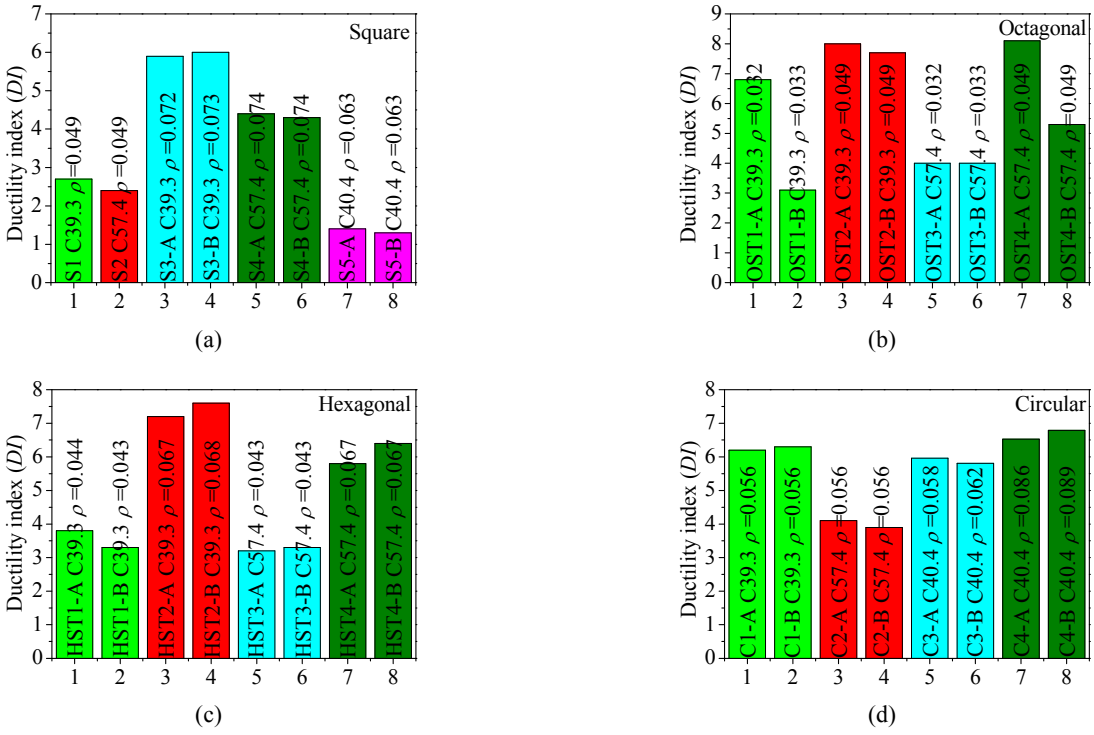

Fig. 6 Comparison of ductility index DI for all specimens

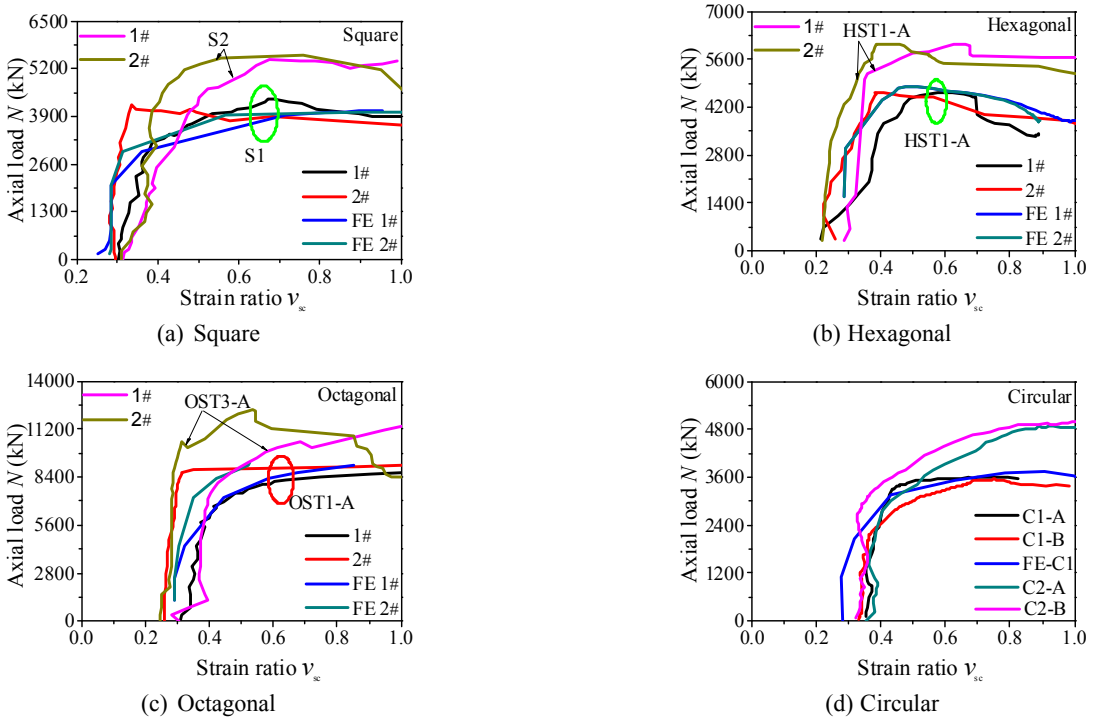

Fig. 7 Comparison of axial load vs. strain ratio curves from experimental and FE results

to the OST3 specimens, the average *DI* of the OST4 specimens was increased by 66.7%, with the same increase in the steel ratio.

In comparison to the OST1 specimens, the average *DI* of the OST3 specimens was reduced by 18.7% with the increase of concrete strength from 39.3 Mpa to 57.4 Mpa. In addition, compared to the OST2 specimens, the average *DI* of the OST4 specimens was decreased by 15%, with the same increase of concrete strength.

From the above analyses, it can be found that the ductility increases with the increase of steel ratio, and a higher concrete strength led to a lower ductility. Taking the ductility into consideration, the novel column with high steel ratio and low-grade concrete is suggested to be used in

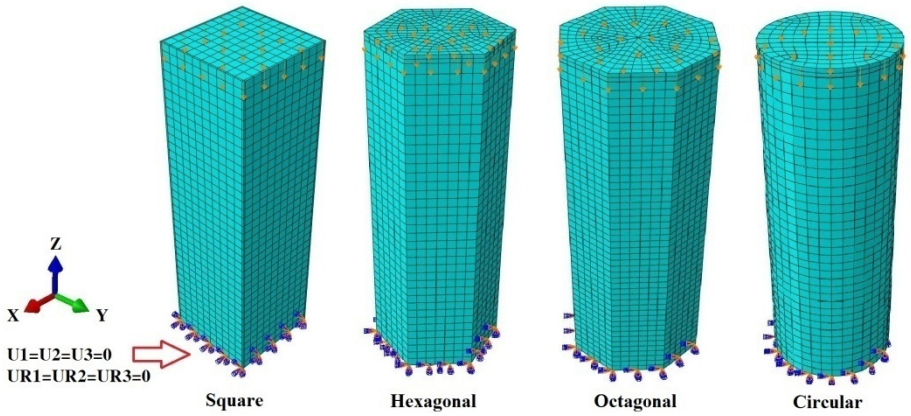

Fig. 8 The meshed FE model

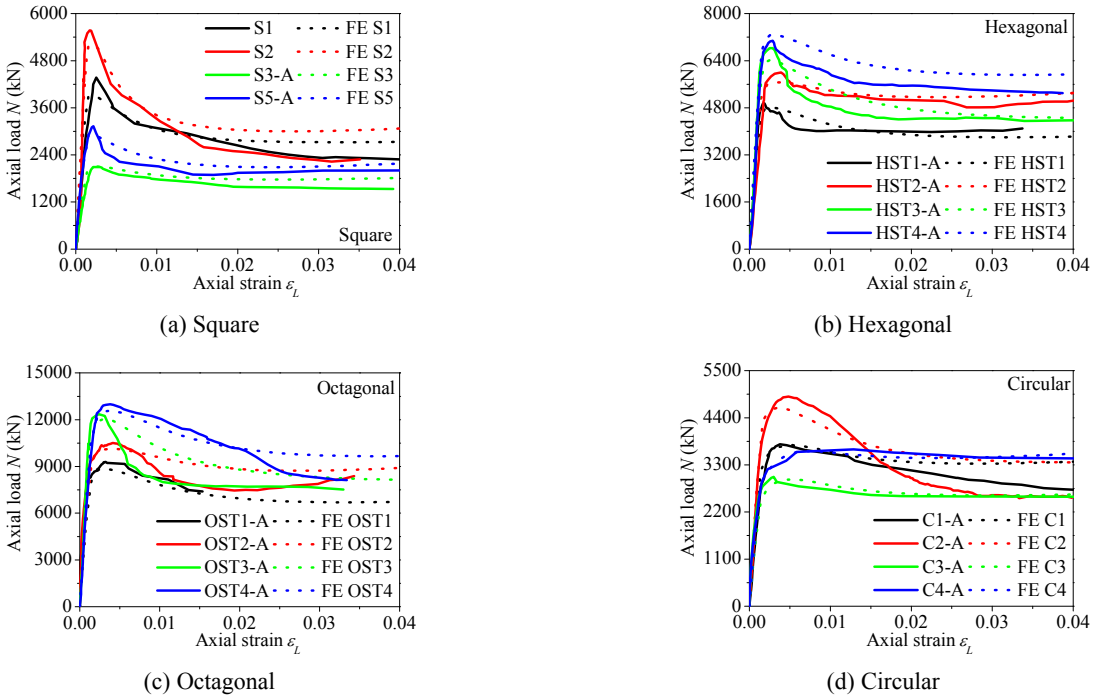

(a) Square (b) Hexagonal

(c) Octagonal (d) Circular

Fig. 9 Comparison of axial load vs. strain curves of specimens between FE and experimental results

engineering practices.

3.4 Strain ratio

The strain ratio (v_{sc}) is defined herein as the absolute value of the circumferential strain divided by the axial strain of the steel tube, which reveals the confinement effect of the steel tube on the core concrete. The more the strain ratio is, the more the confinement effect is between core concrete and steel tube. Fig. 7 shows the relationship of the strain ratio (v_{sc}) of the steel tube to the axial load (N).

As can be seen from Fig. 10, the strain ratio was nearly constant and approximately equivalent to Poisson's ratio of steel at the initial stage, indicating that there is negligible confinement effect of the steel tube on the core concrete. When reaching about 60% of the ultimate bearing capacity, the strain ratio began to increase sharply and was larger than the Poisson's ratio. The change in strain indicated the steel tube produces a significant confinement effect on the core concrete. For CFT stub column with circular cross-section, the cross-section is symmetric at any angle, so the strain ratio of the steel tube at any points is the same. In addition, for CFT stub column with other cross-sections, the strain ratio at endpoint was greater than that in other points under the same compressive load, indicating the confinement effect of the steel tube on the core concrete at the end point was optimal, followed by other points.

4. Finite element (FE) modeling

4.1 FE models

FE models were established by the commercial software ABAQUS/Standard 6.10 (Hibbitt *et al*. 2003), which has been extensively adopted to investigate the composites

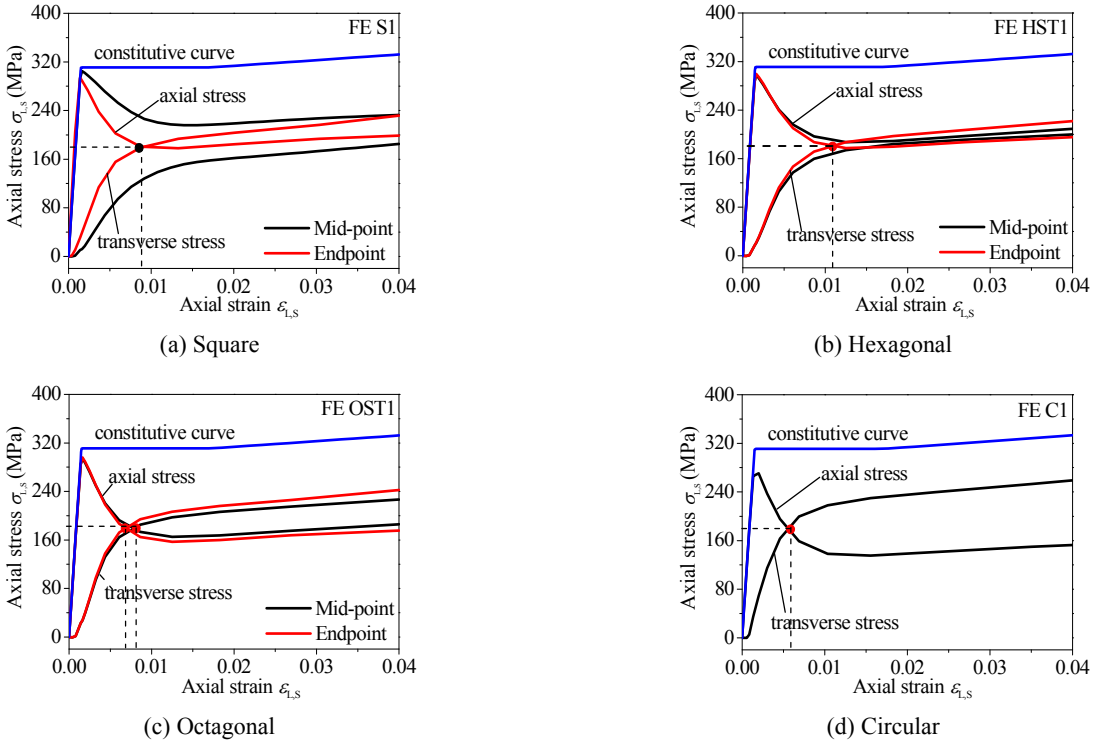

(a) Square (b) Hexagonal

(c) Octagonal (d) Circular

Fig. 10 The stress vs. axial strain curves at the different points of the steel tube

structures (Chang *et al*. 2013, 2014, Wan and Zha 2016). In these models, the 8-node reduced integral format 3D solid element (C3D8R) was used to model the core concrete, steel tube and loading plates for all specimens. The structured meshing technique was adopted as shown in Fig. 8.

A surface-based interaction with hard contact in the normal direction and the Coulomb friction coefficient of 0.5 in the tangential direction to the interface is used to simulate the interfacial behavior between steel tube and core concrete, in which the sliding formulation is finite sliding. For the surface-based model, selection of coefficient of friction is difficult because there is no standard test procedure to determine it. According to the existing studies (Baltay and Gjelsvik 1990, Dai and Lam 2010, Guo 2003, Hassanein and Kharoob 2014, Wang *et al*. 2017, Xu *et al*. 2016), coefficient of friction used for CFST columns under axial compression ranged from 0.3 to 0.5. In this paper, different friction coefficients ranging from 0.1 to 0.7 was selected to explore their effects on column behaviors. The results indicates that friction coefficient plays little role in column behavior. A convergent problem was induced when the friction coefficient was greater than 0.8. Therefore, for the surface-based model, the friction coefficient between steel tube and concrete is taken as 0.5 to achieve a quick convergence, which has been proven to be rational in the prior research (Ding *et al*. 2011, 2014 and2017). A tie constraint may couple two separate surfaces so that no relative motion occurs between them. Therefore, the tie option was adopted for the constraint between the steel tube, core concrete and loading plate to ensure that the load is applied to the specimen during the whole loading process.

4.2 Material models

A constitutive model of concrete in CFT columns has been presented by Ding *et al*. (2011) through modifying the concrete model under tri-axial loading given by Ottosen and Ristinmaa (2005). The following stress-strain relationship is adopted in the model.

$$y = \begin{cases} \dfrac{Ax + (B-1)x^2}{1 + (A-2)x + Bx^2} & x \le 1 \\ \dfrac{x}{\alpha(x-1)^2 + x} & x > 1 \end{cases} \tag{2}$$

where $y = \sigma/f_c$ and $x = \varepsilon/\varepsilon_c$ are the stress and strain ratios of the core concrete to the uniaxial compressive concrete respectively. σ and ε are the stress and strain of the core concrete. $f_c = 0.4 f_{cu} 7/6$ is the uniaxial compressive strength of concrete, where f_{cu} is the compressive cubic strength of concrete. ε_c is the strain corresponding with the peak compressive stress of concrete, where $\varepsilon_c = 383\, f_{cu}\, 7/18 \times 10^{-6}$. The parameter A is the ratio of the initial tangent modulus to the secant modulus at peak stress and equals to $9.1\, f_{cu}^{-4/9}$. $B = 1.6(A\text{-}1)^2$ is a parameter that controls the decrease in the elastic modulus along the ascending branch of the axial stress-strain relationship. For a concrete-filled steel tubular stub column, parameter α can be taken as 0.15. More information of the concrete model could be referred in Ding *et al*. (2011, 2014).

The concrete damaged plasticity model defined in ABAQUS has been verified by experimental results (Ding *et al*. 2011, 2014, Liu *et al*. 2016). The parameters presented by Ding *et al*. (2011) included: the eccentricity is 0.1; the ratio of initial equibiaxial compressive yield stress

to initial uniaxial compressive yield stress (f_{b0}/f_{c0}) is 1.225; the ratio of the second stress invariant on the tensile meridian to that on the compressive meridian is 2/3; the viscosity parameter is 0.005; and the dilation angle (θ) is 40°. Therefore, the concrete damaged plasticity model is adopted to investigate the behavior of SRCFT stub columns in this paper.

According to a great number of experimental studies on the material properties of steel, an elasto-plastic model, considering Von Mises yield criteria, Prandtl-Reuss flow rule, and isotropic strain hardening, is used to describe the constitutive behavior of steel. The expression for the stress-strain relationship of the steel is described as follow (Ding *et al*. 2011).

$$\sigma_i = \begin{cases} E_s \varepsilon_i & \varepsilon_i \le \varepsilon_y \\ f_y & \varepsilon_y < \varepsilon_i \le \varepsilon_{st} \\ f_y + \zeta E_s(\varepsilon_i - \varepsilon_{st}) & \varepsilon_{st} < \varepsilon_i \le \varepsilon_u \\ f_u & \varepsilon_i > \varepsilon_u \end{cases} \quad (3)$$

where, σ_i and ε_i are the equivalent stress and strain of the steel. f_y, and f_u (= 1.5 f_y) are the yield strength and ultimate strength respectively. E_s (= 2.06×10^5 MPa) and E_{st} (E_{st} = ζE_s) are the elastic modulus and strengthening modulus. ε_y, ε_{st} and ε_u are the yield strain, hardening strain, and ultimate strain of steel, which is described by $\varepsilon_u = \varepsilon_{st} + 0.5 f_y/(\zeta E_s)$, where ε_{st} =12ε_b, ε_u = 120ε_b and ζ = 1/216.

To model the descending stage of load-bearing capacity of specimens, load was applied by means of displacement. And both material and structural nonlinearities were considered and solved using the incremental-interactive method in ABAQUS.

4.3 Experimental verification

According to the material model and boundary condition as mentioned above, the feasibility and accuracy of the FE models were verified by comparing the experimental and FE results in this section. The comparisons between the experimental and FE results is listed in Table 3. Good agreements are achieved and the discrepancies between the experimental and FE results are less than 11% for all the specimens. Fig. 9 shows the comparisons of the axial load vs. strain curves between experimental and FE results. The results indicate that the predicted curves agree well with the experimental results, especially for the elastic stage and ultimate bearing capacity. Besides, the accuracy of the FE modeling approach was further verified by the comparison of the axial load vs. strain curves between the experimental and FE results, as shown in Fig. 7. It can be seen from the Fig. 7 that the experimental results are in agreement with FE results. With such confirmed validation, the material constitutive model adopted in this study and the FE model approaches using ABAQUS were reasonable and adequate.

4.4 Composite action analysis

To obtain further understanding on the mechanical performances of the polygonal CFT stub columns under axial loading, the composite action between the steel tube and core concrete is investigated in this section.

The axial and transverse stress vs. strain curves for the steel tube at different points is shown in Fig. 10. According to Ding *et al*. (2014), the stress vs. strain curve in the steel tube can reflect the confinement effect. If the axial stress vs. strain curves in the steel tube crosses the transverse one, it indicates that the steel tube can provide a high confinement

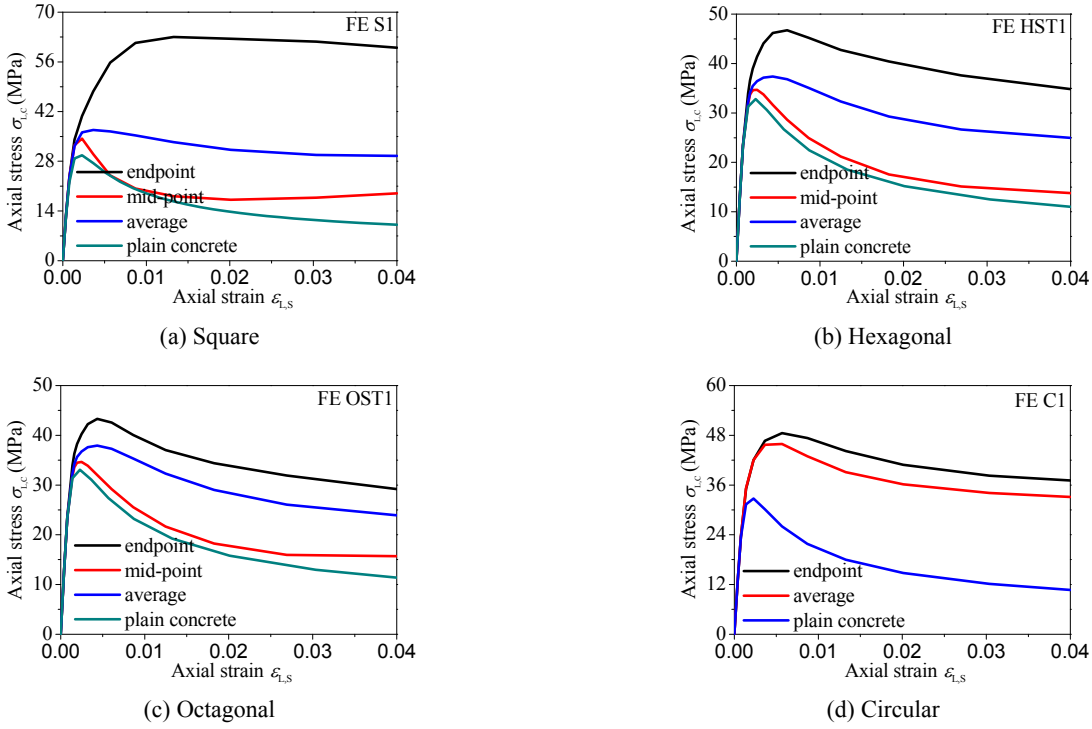

(a) Square (b) Hexagonal

(c) Octagonal (d) Circular

Fig. 11 Comparison of axial stress vs. strain curves at the different points of the core concrete

effect on the core concrete.

As can be seen in Fig. 10, the axial stress and transverse stress of the steel tube at endpoint has intersection, but has no intersection at mid-point, or the intersection at mid-point appears later than that at endpoint. That is to say that the confinement effect of the steel tube on the core concrete at endpoint is obviously greater than that at mid-point. In addition, for the circular CFT stub columns, the confinement effect of the steel tube on the core concrete is the same at any points.

Fig. 11 gives axial stress-strain curves of the core concrete on the half height of the specimens. It can be found that the compressive strength of the core concrete for CFT stub columns is much greater than the plain concrete without the confinement effect. In addition, the compressive strength of the core concrete at endpoint is higher than that at mid-point, which indicated that the steel tube at the end point provided more confinement effect on the core concrete than that at mid-point. The result from Fig. 10 coincides with that from Fig. 11.

4.5 Analysis of the different cross-sections

The change of the cross-section is a special characteristic of the polygonal CFT stub columns and a marked difference compared with common CFT stub columns. The influence of varied cross-section on the behavior of CFT stub columns is discussed in detail in this section. For the convenience of comparison and analysis, the equivalent area method is adopted to investigate the effect of different cross-sections on the behavior of CFT stub columns. The area of the core concrete and steel tube keep the same (the steel ratio ρ = 0.08), the concrete strength (f_{cu}) and yield strength of the steel (f_y) are 39.3 Mpa and 311 Mpa respectively, while the cross-section is variable. The following will take the specimen as examples

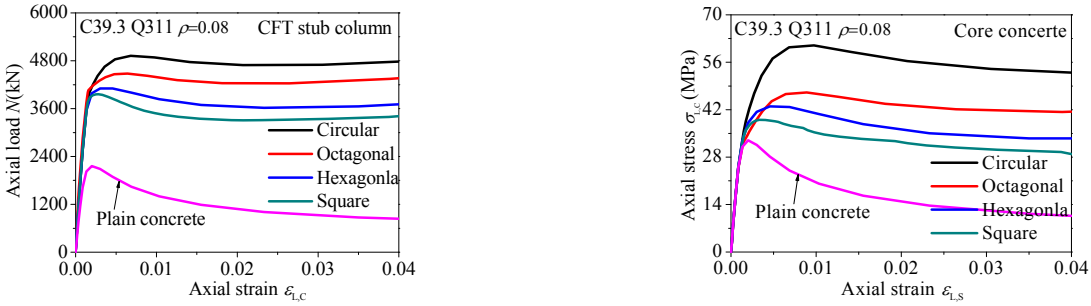

(a) Axial stress vs. strain curves (b) Axial load vs. strain curves

Fig. 12 Comparison of axial load/ stress vs. strain curves

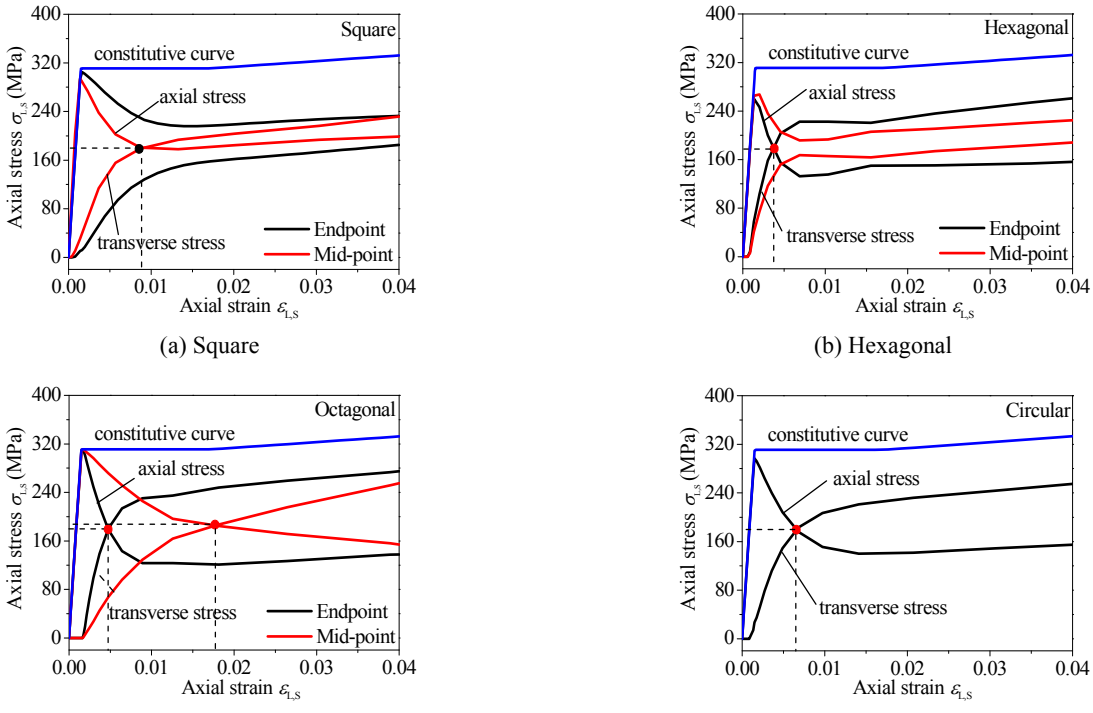

(a) Square (b) Hexagonal

(c) Octagonal (d) Circular

Fig. 13 The stress vs. axial strain curves at the different points of the steel tube

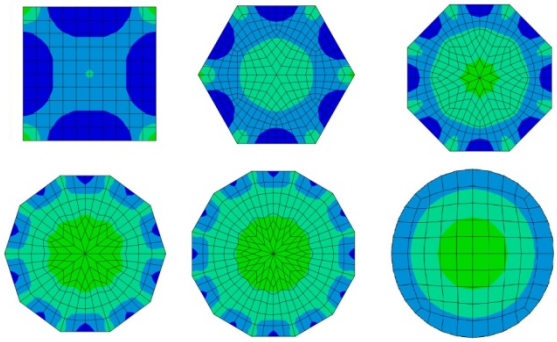

Fig. 14 Comparisons of stress contour at mid-section for the polygonal CFT stub columns

to discuss the behavior of the polygonal CFT stub columns.

Fig. 12 gives the comparisons of the axial load vs. strain curves and the axial stress vs. strain curves for the polygonal CFT stub columns, respectively. It is obvious that the strength of CFT stub columns is significantly greater than the plain concrete due to the confinement effect of the steel tube on the core concrete. The curve of the plain concrete declines more quickly after peak load than other curves due to without the confinement effect of the steel tube, which leads to a weaker ductility. In addition, the compressive stiffness of all the specimens remained the same at the elastic stage with the increase in the number of edges of cross-section, while the ultimate bearing capacity gradually increased, where that of the circular CFT stub column is highest, followed by the octagonal, hexagonal and square CFT stub column, respectively.

Fig. 13 gives the axial and transverse stress vs. strain curves of the steel tube at different points for the polygonal CFT stub columns, respectively. Based on the careful observation of the axial and transverse stress vs. strain curves for the polygonal CFT stub columns, the following four Figs can reflect such tendency. Firstly, the confinement effect of the steel tube on the core concrete at endpoint is greater than that at mid-point. What's more, the distance between the axial stress-strain curves and the transverse stress vs. strain curves gradually reduces with the change of the cross-section. When CFT stub column tends to be the circular cross-section, the intersection between the axial stress and transverse stress of the steel tube at mid-point begins to appear, and intersections at the end point and mid-point overlap finally, indicating that CFT stub column is the circular cross-section.

Fig. 14 gives the stress distribution of the core concrete for the polygonal CFT stub columns, respectively. For the polygonal CFT stub columns, the core concrete can be divided into the constrained area and unconstrained area of the core concrete, where the navy blue represents the unconstrained area of the core concrete. It can be seen from Fig. 14 that with the increase in the number of the edges, the constrained area of the core concrete increases gradually and tends to the circular cross-section. In addition, when n (the number of the edges) is equal to 10, the unconstrained area of the core concrete is very limited and nearly equivalent to 0. Therefore, when $n \geq 10$, the polygonal CFT stub columns can be considered to approximately equivalent to the circular CFT stub column.

Through combined the experimental (Fig. 4) and FE results (Fig. 14), it can be found that the failure modes of the steel tube are local buckling, which is associated with the core concrete. The deformation of the local buckling in the unconstrained area of the core concrete is greater than that in the constrained area of the core concrete, because the confinement effect of the steel tube on the core concrete at endpoint is higher than that at mid-point. The result from Fig. 4 coincides with that from Fig. 14. With the increase in the number of edges, the unconstrained area of the core concrete gradually decreases, the deformation of the local buckling of the steel tube is reduced, which results in enhancing the strength of CFT stub columns. What's more, the local buckling in the unconstrained area of the core concrete occurs more easily than that in the unconstrained area of the core concrete. Hence, the results illustrate that the behavior of CFT stub columns changes with the change of the cross-section, and the change is continuous.

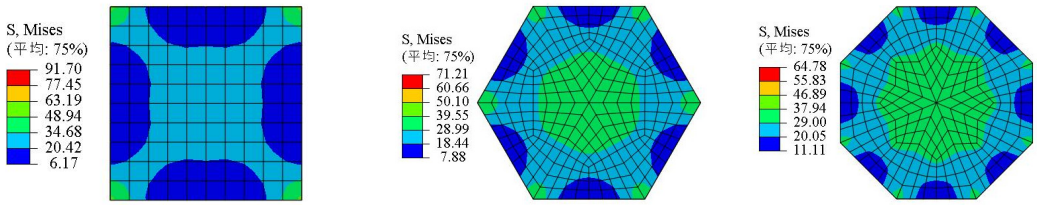

Fig. 15 Comparisons of stress contour at mid-section for the polygonal CFT stub columns

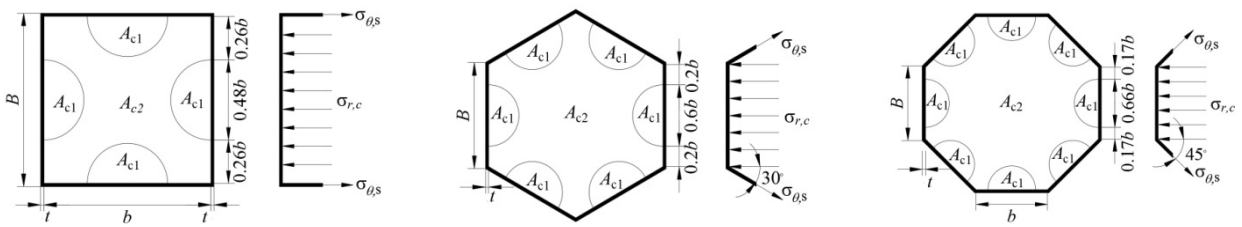

Fig. 16 Simplified stress distribution with the mid-section of the polygonal CFT stub columns

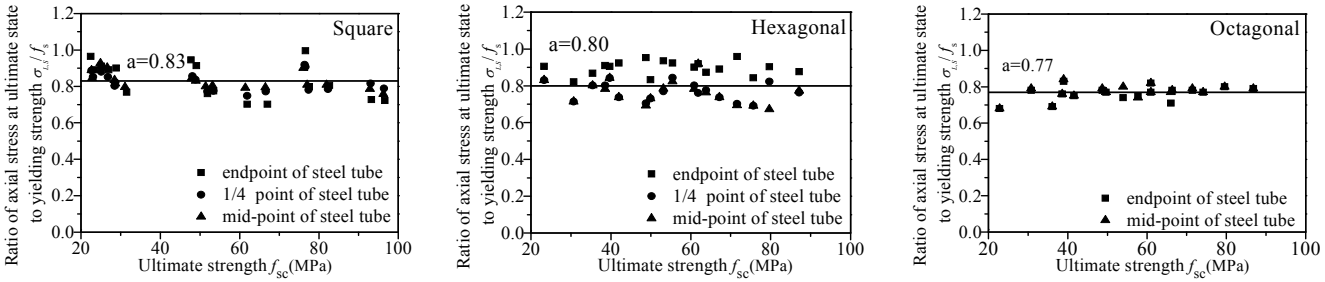

Fig. 17 Average ratio of axial compressive stress to yield stress of the steel tube

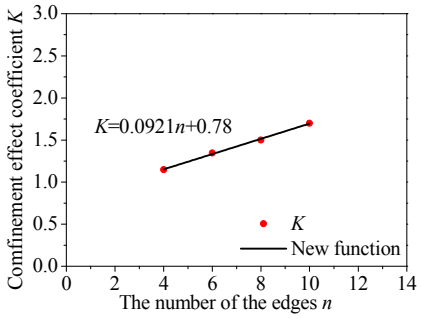

Fig. 18 Relationship between n and K

5. Design approach

Current design methods are applicable for CFT stub columns with circular or square cross-section, but the polygonal CFT stub columns were not covered. On the basis of the above analysis, this paper is an attempt to establish a unified formula for the polygonal CFT stub columns.

5.1 Model simplification

The stress contour at the ultimate state for the polygonal CFT stub columns is extracted from the FE model, as shown in Fig. 15. According to the above figure, the stress distribution of the polygonal CFT stub columns can be simplified as Fig. 16.

This is completely based on stress distribution and the superposition principle of the concrete section at the ultimate state, where A_{c1} is the unconstrained area of core concrete, A_{c2} is the constrained area of core concrete and A_c is the cross-sectional area of core concrete. In this way, the following relations can be expressed

$$\begin{cases} A_{c1}+A_{c2}=A_c \\ A_{c1}=(0.42-0.015\cdot n)A_c, \quad 4\le n\le 8 \\ A_{c2}=(0.58+0.015\cdot n)A_c \end{cases} \tag{4}$$

where, when $n \ge 10$, $A_{c2} = A$, $A_{c1} = 0$.

5.2 Formulation

Based on the validated FE models, parametric study, including steel ratio, concrete strength and steel yield strength, are extensively investigated the behavior of the polygonal CFT stub columns. A total of 54 FE models are established to analyze the following parameters: the steel ratio from 0.02 to 0.1, the concrete strength covering from C40 to C100, the steel yield strength ranging from Q235 to Q420, which are chosen based on the engineering practice.

When the modeling results of load-strain responses reached the ultimate state (i.e., maximum load-bearing capacity), longitudinal stress at three points of the steel tube (endpoint, 1/4 point and mid-point of middle section) are obtained. And the relationship between axial stress yield strength ratio and the specimen's ultimate strength ($f_{sc} = N_u/A_{sc}$, where $A_{sc} = A_c + A_s$ is the total area of cross-section) is shown as Fig. 17, where $\sigma_{L,s}$ is the axial stress of the steel tube.

It can be seen from Fig. 17 that when the polygonal CFT stub columns reach their ultimate strength, the average ratio of the axial compressive stress to the yield stress of steel tube is

$$\begin{cases} \sigma_{L,s}=0.83f_y & n=4 \\ \sigma_{L,s}=0.80f_y & n=6 \\ \sigma_{L,s}=0.77f_y & n=8 \end{cases} \tag{5}$$

Based on Von Mises yield criterion mentioned, the tensile transverse stress ($\sigma_{\theta,s}$) of the steel tube can be obtained as

$$\begin{cases} \sigma_{\theta,s}=0.28f_y & n=4 \\ \sigma_{\theta,s}=0.32f_y & n=6 \\ \sigma_{\theta,s}=0.36f_y & n=8 \end{cases} \tag{6}$$

As shown in Fig. 16, the relationship between the radial concrete stress ($\sigma_{r,c}$) of the core concrete and the transverse stress of the steel tube ($\sigma_{\theta,s}$) can be expressed as

$$\begin{cases} \sigma_{r,c}=\dfrac{2t}{b}\sigma_{\theta,s} & n=4 \\ \sigma_{r,c}=\dfrac{\sqrt{3}t}{b}\sigma_{\theta,s} & n=6 \Rightarrow \sigma_{r,c}=\dfrac{t\cdot\sigma_{\theta,s}}{b}\cos\theta \\ \sigma_{r,c}=\dfrac{\sqrt{2}t}{b}\sigma_{\theta,s} & n=8 \end{cases} \tag{7}$$

The axial compressive strength ($\sigma_{L,c}$) of the core concrete can be obtained as follow

$$\sigma_{L,c} = f_c + p\sigma_{r,c} \tag{8}$$

where p is the lateral pressure coefficient, $p = 3.4$ according

Table 3 Comparisons of the bearing capacity obtained from experimental, FE and predicted results

Specimen ID	Source	$N_{u,Exp}$	$N_{u,c}$				$N_{u,Exp}/N_{u,c}$			
		Exp	FE	Eq.12	GB	EC	FE	Eq.12	GB	EC
S1	This paper	4370	3931	4068	4325	3863	1.11	1.07	1.01	1.13
S2		5570	5261	5445	5968	5241	1.06	1.02	0.93	1.06
S3-A		2160	2078	2126	2196	1990	1.04	1.02	0.98	1.09
S3-B		2090	2078	2126	2196	1990	1.01	0.98	0.95	1.05
S4-A		2500	2732	2722	2899	2587	0.92	0.92	0.86	0.97
S4-B		2610	2732	2722	2899	2587	0.96	0.96	0.90	1.01
S5-A		3131	2939	3147	3300	2968	1.07	1.00	0.95	1.05
S5-B		2832	2939	3147	3300	2968	0.96	0.90	0.86	0.95
HST1-A		4806	4947	4717		4260	1.03	1.05		1.16
HST1-B		4902	4618	4717		4260	0.94	0.98		1.08
HST2-A		5666	6001	5762		5028	1.06	1.04		1.19
HST2-B		5724	6041	5762		5028	1.06	1.05		1.20
HST3-A		6423	6827	6326		5868	1.06	1.08		1.16
HST3-B		6482	6803	6326		5868	1.05	1.08		1.16
HST4-A		7280	7079	7325		6590	0.97	0.97		1.07
HST4-B		7067	7289	7325		6590	1.03	1.00		1.11
OST1-A		9297	8942	8698	8780	7715	1.04	0.94	1.06	1.20
OST1-B		9311	8850	8698	8780	7715	1.05	0.95	1.06	1.21
OST2-A		10502	10128	11177	9390	8226	1.04	0.99	1.12	1.28
OST2-B		10713	9800	11177	9390	8226	1.09	1.01	1.14	1.30
OST3-A		12362	12048	10724	11086	9700	1.03	1.04	1.12	1.27
OST3-B		12357	11906	10724	11086	9700	1.04	1.04	1.11	1.27
OST4-A		12992	12582	13099	11644	10190	1.03	1.03	1.12	1.27
OST4-B		13263	12787	13099	11644	10190	1.04	1.05	1.14	1.30
C1-A		3780	3339	3806	3694	3040	1.13	0.99	1.02	1.24
C1-B		3540	3339	3806	3694	3040	1.06	0.93	0.96	1.16
C2-A		4896	4640	4887	4939	4121	1.06	1.00	0.99	1.19
C2-B		4976	4640	4887	4939	4121	1.07	1.02	1.01	1.21
C3-A		3023	2962	2974	2832	2319	1.02	1.02	1.07	1.30
C3-B		3265	2933	2974	2832	2319	1.11	1.10	1.15	1.41
C4-A		3556	3634	3560	3266	2645	0.98	1.00	1.09	1.34
C4-B		3661	3623	3560	3266	2645	1.01	1.03	1.12	1.38
					Average		1.03	1.01	1.03	1.18
					COV		0.047	0.048	0.088	0.098

to Ding *et al*. (2011).

The ultimate bearing capacity (N_u) of axially-loaded polygonal CFT stub columns can therefore be expressed as

$$N_u = \sigma_{L,c} A_{c2} + f_c A_{c1} + \sigma_{L,s} A_s \tag{9}$$

where A_s is the cross-sectional area of the steel tube.

Substituting Eqs. (4)-(8) into Eq. (9), based on existing design method on the circular CFT stub columns (Ding *et al*. 2017), the ultimate bearing capacity (N_u) can be described as

$$N_u = f_c A_c (1 + K\Phi) \tag{10}$$

where Φ is the confinement index and is defined by $\Phi = f_y A_s / f_c A_c$.

Fig. 18 gives the effect of the number of edges (n) on the coefficient K. And the relationship between n and K of CFT stub columns can be obtained by regression analysis.

$$K = 0.921 \cdot n + 0.78 \tag{11}$$

Therefore, the ultimate bearing capacity of the polygonal CFT stub columns under axial loading (N_u) can be expressed as followed

$$N_u = f_c A_c (1 + (0.921 \cdot n + 0.78)\Phi \tag{12}$$

Table 4 Formulas for bearing capacity of the polygonal CFT stub column

Reference	Formulation
GB 50936-2014 (2014)	$N_u = A_{sc}(1.12 + B\theta + C\theta^2) f_c, \theta = \frac{A_s f_y}{A_c f_c}$
Eurocode 4 (2004)	$N_u = A_c f_c + A_s f_y$

where $4 \le n \le 10$. When n (the number of edges) ≥ 10, the confinement coefficient of the polygonal CFT stub columns is calculated according to the circular cross-section, and is equal to 1.7.

5.3 Formula validation

The predicted results ($N_{u,c}$) using different formulas (Eq. (12)) are compared to the experimental results ($N_{u,\,Exp}$), as shown in Table 3, in which the ratios are values of experimental results divided by the corresponding predicted values. Different formulas available in the standards for predicting the strength of the polygonal CFT stub columns are summarized in Table 4.

It can be seen that the average ratios of $N_{u,\,Exp}/N_{u,\,FE}$, $N_{u,\,Exp}/N_{u,\,Eq.(12)}$, $N_{u,\,Exp}/N_{u,GB}$ and $N_{u,\,Exp}/N_{u,\,EC4}$ are 1.03, 1.01, 1.03, and 1.18 with a coefficient of variation of 0.047, 0.048, 0.088, and 0.098, respectively. It can be found that the proposed formula Eq. (12) in this paper ensured the same accuracy level as the standard GB 5936-2014 (2014), while it is much simpler in engineering practices and the standard GB 5936-2014 (2014) don't cover CFT stub columns with the hexagonal cross-section. In addition, the Eurocode 4 (2004) significantly underestimates the bearing capacity and the maximum deviation reaches about 41%, because the confinement effect of the steel tube on the core concrete was neglected. Hence, Eq. (12) can be adopted as the fundamental formula to predict the ultimate bearing capacity of the polygonal CFT stub columns.

6. Conclusions

This paper presents a combined experimental and numerical study on the behavior of the polygonal CFT stub columns under axial loading. Parametric studies are also conducted to investigate the effect of some key parameters on the performance of the polygonal CFT stub columns. Based on the studies and analysis, the main conclusions from this study can be drawn as below.

(1) Experimental results suggest that the concrete strength and steel ratio have effect on both ultimate bearing capacity and the ductility. With the increase of concrete strength, the ultimate bearing capacity of composite columns increases significantly, while the ductility decreased. Increasing the steel ratio can improve both the ultimate bearing capacity and ductility of CFT stub columns.
(2) Based on the axial load vs. strain curves, the specimens are considered to experience three stages until failure: elastic stage, elastic-plastic stage and plastic stage. Besides, the failure modes of composite columns are discussed in detail. Two obvious local buckling appears at different heights on the opposite sides of the steel tube, which results in a visible shear plane occurred between the local buckling.
(3) FE models are established to investigate the behavior of CFT stub columns based on the reasonable material constitutive model, which is well in agreement with the experimental results.
(4) The FE results show that the steel tube provides a higher confinement effect on the core concrete, and the confinement effect at endpoint is greater than that at mid-point. In addition, the confinement effect of the steel tube on the core concrete increases gradually with the increase of edges, while the deformation of the local buckling decreases. The behavior of CFT stub columns changes with the change of the cross-section, and the change is in continuity.
(5) A simplified and unified formula for calculating the bearing capacity of the polygonal CFT stub column is proposed based on the limit equilibrium method with ration simplification. The predicted results using the proposed formula agree well with experimental results. Therefore, this formula can be adopted as the basic form to estimate the strength of the polygonal CFT stub column in practice engineering.

Acknowledgments

This research work was financially supported by the National Natural Science Foundation of China, Grant No. 51578548 and 51508294, and the National Key Research program of China, Grant No.2017YFC0703404.

References

Aslani, F., Uy, B., Tao, Z. and Mashiri, F. (2015), "Predicting the axial load capacity of high-strength concrete filled steel tubular columns", *Steel Compos. Struct., Int. J.*, **19**(4), 967-993.

Baltay, P. and Gjelsvik, A. (1990), "Coefficient of friction for steel on concrete at high normal stress", *J. Mater. Civil Eng.*, **2**(1), 46-49.

Chang, X., Ru, Z.L., Zhou, W. and Zhang, Y.B. (2013), "Study on concrete-filled stainless steel carbon steel tubular (CFSCT) stub columns under compression", *Thin-Wall. Struct.*, **63**(2), 125-133.

Chang, X., Luo, X.L., Zhu, C.X. and Tang, C.N. (2014), "Analysis of circular concrete-filled steel tube support in high ground stress conditions", *Tunn. Undergr. Sp Tech.*, **43**(6), 41-48.

Dai, X. and Lam, D. (2010), "Numerical modeling of the axial compressive behaviour of short concrete-filled elloptical steel columns", *J. Constr. Steel Res.*, **66**, 931-42.

Ding, F.X., Ying, X.Y., Zhou, L.C. and Yu, Z.W. (2011), "Unified calculation method and its application in determining the uniaxial mechanical properties of concrete", *Front. Archit. Civ. Eng. China.*, **5**(3), 381-393.

Ding, F.X., Fang, C.J., Bai, Y. and Gong, Y.Z. (2014), "Mechanical

performance of stirrup-constrained concrete-filled steel tubular stub columns under axial loading", *J. Constr. Steel Res.*, **98**(11), 146-157.

Ding, F.X., Tan, L., Liu, X.M. and Wang, L.P. (2017), "Behavior of circular thin-walled steel tube confined concrete stub columns", *Steel Compos. Struct., Int. J.*, **23**(2), 229-238.

El-Heweity, M.M. (2012), "On the performance of circular concrete-filled high strength steel columns under axial loading", *Alexandria Eng. J.*, **51**(2), 109-119.

Ellobody, E. (2013a), "Numerical modeling of fibre reinforced concrete-filled stainless steel tubular columns", *Thin-Wall. Struct.*, **63**(2), 1-12.

Ellobody, E. (2013b), "Nonlinear behavior of eccentrically loaded FR concrete-filled stainless steel tubular columns", *J. Constr. Steel Res*, **90**(11), 1-12.

Eurocode 4, European standard (2004), *Design of Composite Steel and Concrete Structures Part1-1: General Rules-Structural Rules for Buildings*, European Committee for Standardization, Brussels, EN 1994-1-2.

Evirgen, B., Tuncan, A. and Taskin, K. (2014), "Structural behavior of concrete filled steel tubular sections (cft/cfst) under axial compression", *Thin-Wall. Struct.*, **80**(9), 46-56.

GB/T228-2002, China Standard (2002), *Metallic materials-tensile testing at ambient temperatures*, Standards Press of China, Beijing, China.

GB/T50081-2002, China Standard (2002), *Standard for method of mechanical properties on ordinary concrete*, China Building Industry Press, Beijing, China.

GB 50017-2003, China Standard (2003), *Code for design of steel structures*, China Planning Press, Beijing, China.

GB 5936-2014, China Standard (2014), *Technical Code for Concrete Filled Steel Tubular Structures*, China Building Industry Press, Beijing, China.

Guo, Z.H. (2003), "Strength and constitutive relation of concrete", Chinese Building Industry Press, Beijing, China.

Hassanein, M.F. and Kharoob, O.F. (2014), "Analysis of circular concrete-filled double skin tubular slender columns with external stainless steel tube", *Thin-Wall. Struct.*, **79**(6), 23-37.

Hassanein, M.F., Kharoob, O.F. and Liang, Q.Q. (2013), "Circular concrete-filled double skin tubular short columns with external stainless steel tubes under axial compression", *Thin-Wall. Struct.*, **73**(12), 252-263.

Hibbitt, Karlson & Sorensen Inc. (2003), ABAQUS/standard User's Manual, Version 6.4.1., Pawtucket, RI, USA.

Hua, W., Wang, H.J. and Hasegawa, A. (2014), "Experimental study on reinforced concrete filled circular steel tubular columns", *Steel. Compos. Struct., Int. J.*, **17**(4), 517-533.

Huang, F.Y., Yu, X.M. and Chen, B.C. (2012), "The structural performance of axially loaded CFST columns under various loading conditions", *Steel Compos. Struct., Int. J.*, **13**(5), 451-471.

Jamaluddin, N., Lam, D., Dai, X.H. and Ye, J. (2013), "An experimental study on elliptical concrete filled columns under axial compression", *J. Constr. Steel Res.*, **87**(8), 6-16.

Kim, J.K., Kwak, H.G. and Kwak, J.H. (2013), "Behavior of Hybrid Double Skin Concrete Filled Circular Steel Tube Columns", *Steel Compos. Struct., Int. J.*, **14**(14), 191-204.

Liang, Q.Q. (2017), "Nonlinear analysis of circular double-skin concrete-filled steel tubular columns under axial compression", *Eng. Struct.*, **131**, 639-650.

Liu, J., Ding, F.X., Liu, X.M. and Yu, Z.W. (2016), "Study on flexural capacity of simply supported steel-concrete composite beam", *Steel Compos. Struct., Int. J.*, **21**(4), 829-847.

Ottosen, N.S. and Ristinmaa, M. (2005), "12-Common Plasticity Models", *Mech. Constitut. Model.*, 279-319.

Pagoulatou, M., Sheehan, T., Dai, X.H. and Lam, D. (2014), "Finite element analysis on the capacity of circular concrete-filled double-skin steel tubular (CFDST) stub columns", *Eng. Struct.*, **72**, 102-112.

Park, J.W. and Choi, S.M. (2013), "Structural behavior of CFRP strengthened concrete-filled steel tubes columns under axial compression loads", *Steel. Compos. Struct., Int. J.*, **14**(5), 453-472.

Tao, Z., Wang, Z.B. and Yu, Q. (2013), "Finite element modelling of concrete-filled steel stub columns under axial compression" *J. Constr. Steel Res.*, **89**(5), 121-131.

Uenaka, K. (2014), "Experimental study on concrete filled elliptical/oval steel tubular stub columns under compression", *Thin-Wall. Struct.*, **78**(5), 131-137.

Wan, C.Y. and Zha, X.X. (2016), "Nonlinear analysis and design of concrete-filled dual steel tubular columns under axial loading", *Steel Compos. Struct., Int. J.*, **20**(3), 571-597.

Wang, Q.T. and Chang, X. (2013), "Analysis of concrete-filled steel tubular columns with "T" shaped cross section (CFTTS)", *Steel Compos. Struct., Int. J.*, **15**(1), 41-45.

Wang, Z.B., Tao, Z., Han, L.H., Uy, B., Lam, D. and Kang, W.H. (2017), "Strength, stiffness and ductility of concrete-filled steel columns under axial compression", *Eng. Struct.*, **135**, 209-221.

Xiamuxi, A. and Hasegawa, A. (2011), "Compression test of RCFT columns with thin-walledsteel tube and high strength concrete", *Steel. Compos. Struct., Int. J.*, **11**(5), 391-402.

Xu, W., Han, L.H. and Li, W. (2016), "Performance of hexagonal cfst members under axial compression and bending", *J. Constr. Steel Res.*, **123**, 162-175.

Yang, Y., Wang, Y. and Fu, F. (2014), "Effect of reinforcement stiffeners on square concrete-filled steel tubular columns subjected to axial compressive load", *Thin-Wall. Struct.*, **82**(9), 132-144.

Yuan, W.B. and Yang, J.J. (2013), "Experimental and numerical studies of short concrete-filled double skin composite tube columns under axially compressive loads", *J. Constr. Steel Res.*, **80**(1), 23-31.

Zha, X., Gong, G. and Liu, X. (2013), "Study on behavior of concrete filled elliptical steel tube members part I: short and long columns under axial compression", *Adv. Steel Constr.*, **9**(2), 90-107.

CC